Ilkka Nissilä, Tommi Noponen, Kalle Kotilahti, Toivo Katila, Lauri Lipiäinen, Tanja Tarvainen, Martin Schweiger, and Simon Arridge. 2005. Instrumentation and calibration methods for the multichannel measurement of phase and amplitude in optical tomography. Review of Scientific Instruments, volume 76, number 4, 044302, 10 pages.

Instrumentation and calibration methods for the multichannel measurement of phase and amplitude in optical tomography

Ilkka Nissilä,[a] Tommi Noponen, Kalle Kotilahti, and Toivo Katila
Laboratory of Biomedical Engineering, Helsinki University of Technology, P.O. Box 2200, FIN-02015, Finland

Lauri Lipiäinen
Cognitive Brain Research Unit, Department of Psychology, University of Helsinki, P.O. Box 9, FIN-00014, Finland

Tanja Tarvainen
Department of Applied Physics, University of Kuopio, P.O. Box 1627 FIN-70211, Finland

Martin Schweiger and Simon Arridge
Department of Computer Science, University College London, Gower Street, London WC1E 6BT, United Kingdom

(Received 27 August 2004; accepted 7 February 2005; published online 23 March 2005)

In this article, we describe the multichannel implementation of an intensity modulated optical tomography system developed at Helsinki University of Technology. The system has two time-multiplexed wavelengths, 16 time-multiplexed source fibers and 16 parallel detection channels. The gain of the photomultiplier tubes (PMTs) is individually adjusted during the measurement sequence to increase the dynamic range of the system by 10^4. The PMT used has a high quantum efficiency in the near infrared (8% at 800 nm), a fast settling time, and low hysteresis. The gain of the PMT is set so that the dc anode current is below 80 nA, which allows the measurement of phase independently of the intensity. The system allows measurements of amplitude at detected intensities down to 1 fW, which is sufficient for transmittance measurements of the female breast, the forearm, and the brain of early pre-term infants. The mean repeatability of phase and the logarithm of amplitude (ln A) at 100 MHz were found to be 0.08° and 0.004, respectively, in a measurement of a 7 cm phantom with an imaging time of 5 s per source and source optical power of 8 mW. We describe a three-step method of calibrating the phase and amplitude measurements so that the absolute absorption and scatter in tissue may be measured. A phantom with two small cylindrical targets and a second phantom with three rods are measured and reconstructions made from the calibrated data are shown and compared with reconstructions from simulated data. © *2005 American Institute of Physics.* [DOI: 10.1063/1.1884193]

I. INTRODUCTION

Optical tomography in medical imaging is a method for the noninvasive imaging of the optical properties of tissue using visible or near-infrared light.[1–3] In the method, light is delivered to tissue using source optodes, which are typically optical fibers, and detected using detector optodes, which are usually fiber bundles transmitting the light to the detectors. The optodes are distributed on the surface of the tissue in such a way that measurements can be made with a variety of source-detector distances. The arrangement of the optodes should be such that the measurements are sensitive to the optical properties of the internal parts of the tissue.

Light propagation in tissue is usually modeled using approximations to the radiative transfer equation, such as the diffusion approximation (DA) which is valid in strongly scattering random media. The optical properties of tissue in the DA model are the absorption coefficient μ_a, the scattering coefficient μ_s', and the index of refraction n. The most clinically useful contrast in optical tomography is due to the wavelength-dependent absorption coefficients of oxy- and deoxyhemoglobin (HbO_2 and Hb). Other absorbers in tissue include water and lipids. Two or more wavelengths may be used to differentiate between the absorbers. The separation of scattering and absorption requires the measurement of several different data types, such as the amplitude and phase of the photon density wave in an intensity-modulated system.[4]

In optical tomography, the light propagation model is used to predict the boundary measurements given a set of internal optical properties. In the inverse problem, the model is used together with nonlinear optimization techniques to generate images of the internal optical properties of the tissue.[1] In this article, we have used a three-dimensional finite element (FE) solver for the DA, and an iterative inversion algorithm developed at University College London to reconstruct images of two phantoms based on measured data.

Instrumentation may be broadly divided into three categories. Time-domain systems[5–9] use short (~ps) pulses of

[a]Author to whom correspondence should be addressed; electronic mail: ilkka.nissila@hut.fi

light and measure the temporal point spread function of the tissue by counting the photons that exit the tissue within discrete time intervals. Frequency-domain (FD) systems[10–16] use radio frequency intensity modulated light sources and measure the phase and amplitude of the detected signal relative to the light source signal. Continuous wave (CW) systems[17–19] use low frequency (~kHz) modulated or pulsed (~ms) light sources and measure the intensity of light exiting the tissue.

The instrument developed in our laboratory is based on the frequency-domain principle. It has 16 time-multiplexed source fibers, 16 parallel detection channels, and two wavelengths. The instrument operates at a modulation frequency of 100 MHz, and the wavelengths used currently in measurements are 760 and 830 nm. The distinctive qualities of the instrument include low noise and a wide dynamic range ($\sim 1:10^6$). It can be calibrated to give absolute measurements, which allow the reconstruction of the optical properties of the tissue without a reference measurement with a homogeneous phantom given sufficient contrast in the optical property distribution of the tissue. The instrument may be used to measure data with a high signal-to-noise ratio (SNR) at close source-to-detector separations, making it useful for detecting small changes in $[HbO_2]$ and [Hb] of activated cortical areas in adults and neonates. The system is suitable for tomographic measurements on the brains of premature neonates, adult female breast tissue, adult forearms, and topographic two-dimensional imaging of the adult and infant cortex.

A high sensitivity and a large dynamic range are necessary for tomographic imaging of thick and optically highly attenuating tissues. Optical tomography of the premature infant head is an example where the dynamic range of current systems limits the head diameter (and age) of the subjects that can be studied. In our implementation, the sensitivity of the system has been improved over previously published frequency-domain systems by minimizing the coupling between the radio frequency signal which modulates the intensity of the laser diode and the light detection system, by minimizing the cross talk between adjacent channels in the amplifier to a negligible level, and by selecting a detector which has a high quantum efficiency in the near infrared. The detector gain is switched during the measurement to allow the amplitude and phase to be measured accurately at a range of detected light levels.

II. IMPLEMENTATION

A. Radio frequency system

The implementation of the rf system is similar to the single-channel design described in our earlier article[15] with a few changes. The receiving mixer in the present 16-channel implementation is of the JMS-2W (+7 dBm LO) type (Mini-Circuits), which is better optimized for the modulation frequency of 100 MHz. The LO drive is derived by dividing the power of a +22 dBm signal into 16 signals using one 1×2 and two 1×8 power splitters. The main diagram of the instrument is given in Fig. 1.

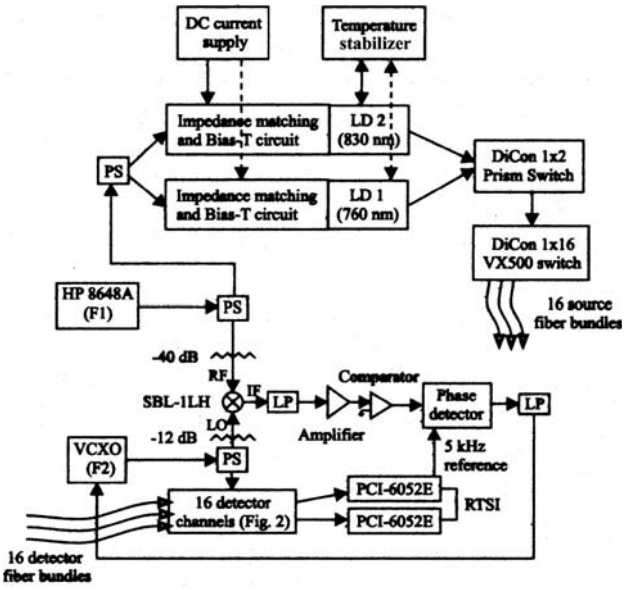

FIG. 1. The main block diagram of the instrument, including the laser diodes, source switches, radio frequency generation system and phase-locked loop. PS=power splitter, LD=laser diode, rf=radio frequency, LO=local oscillator, IF=intermediate frequency, LP=low-pass filter, RTSI=real-time system integration, VCXO=voltage controlled crystal oscillator, F1 =primary modulation frequency, F2=secondary modulation frequency.

B. Phase and amplitude measurement

The digital 16-channel lock-in amplifier was implemented using two multichannel data acquisition cards (National Instruments PCI-6052E). The clocks of the two cards were syncronized using the real-time system integration bus. A programmed counter on the primary card was used to generate the 5 kHz reference signal for the phase-locked loop. The difference frequency between the two primary rf oscillators ($f_1=100.004$ MHz and $f_2=100.009$ MHz) and the 5 kHz transistor-transistor-logic (TTL) reference from the data-acquisition card were phase locked to each other. This intermediate frequency was chosen in such a way that the clock frequency of the data-acquisition cards (20 MHz) is an integral multiple of it. The cards were used in the differential configuration to reduce interchannel cross talk. The raw data were collected at a sample rate of 20 kHz for each channel and converted into phase and amplitude time series in software. The computation time using a third order Chebyshev-type I filter to calculate phase and amplitude for 16 channels is about 13% of the measurement time on a 2.4 GHz Pentium IV PC with a normal priority given to the process, hence a real-time implementation is feasible. The filter coefficients and the output sampling frequency of the lock-in amplifier are user selectable.

C. Light detection

The light is detected by 16 Hamamatsu H6780-20 photosensor modules. The rf signal is amplified by 40 dB using two AMP-75 RF preamplifiers, and the dc component is amplified by 44 dB. The photomultiplier tube (PMT) modules and amplifiers have been enclosed in milled aluminium boxes. The PMT gain is controlled by software. The light detection system is illustrated in Fig. 2.

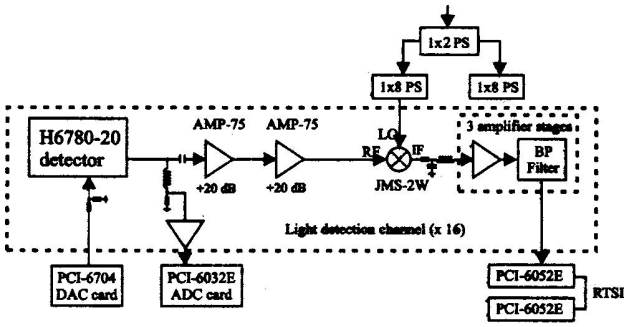

FIG. 2. The light detection unit consisting of the photomultiplier tube with rf and dc amplifiers. DAC=digital-to-analog converter, ADC=analog-to-digital converter, LO=local oscillator, rf=radio frequency, IF=intermediate frequency, PS=power splitter, BP=bandpass, RTSI=real-time system integration.

The isolation provided by the aluminium housings is sufficient so that the shot noise from the PMT exceeds the coupled signal between the source and detector electronics at practical measurement times.

The IF signal from the mixer is amplified further by a multichannel pseudo-differential amplifier which has three noninverting stages. The gain of the third stage is adjusted so that the ratio of the IF amplitudes and the dc anode currents are approximately equal for all the detection channels. The gain of the amplifiers is set so that the maximum rms voltage is approximately 1 V.

D. Light sources

The laser diodes reside in aluminium housings which include thermoelectric cooler (TEC) elements, heat sinks, and a negative-temperature-coefficient resistor.

The PMT high voltages are controlled with a multichannel dc digital-to-analog converter (DAC) card (National Instruments PCI-6704). The dc signal from the PMT is amplified and digitized with a 16-channel analog-to-digital converter (ADC) card (National Instruments PCI-6032E). The dc signals are measured in single-ended mode. The temperature signals from the NTCs are amplified and digitized using a NI PCI-MIO-16XE-50 card. The current through the TEC elements is controlled via two dc DAC channels on the same card.

A commercial 1×2 prism switch (DiCon FiberOptics) is used to select the active wavelength. The light from the switch is then directed to a fiberoptic 1×16 switch (DiCon FiberOptics VX500), which directs the light from the 1×2 to one of the source fibers. The switching times of the 1×2 and 1×16 switches are approximately 10 and 450 ms, respectively. The VX500 has the advantages that it is quiet, highly repeatable, and has low interchannel cross talk. The 1×2 prism switch has been acoustically isolated from the environment.

E. Data acquisition and control software

The data acquision and control software was implemented in C using the LabWindows/CVI environment (National Instruments). The main program selects the active source fiber and wavelength, and sets the high voltage of each detector to the appropriate value for each source-detector pair. The timing and order of the activation of each channel is selected by the user via the use of a sequence file.

To determine the appropriate values for the PMT high voltages for each source and detector pair, a pre-scan is performed before the actual measurement. In the pre-scan, each source fiber and wavelength is activated in turn, and the high voltage of each detector is adjusted from 200 up to 900 V, or until the threshold dc anode current of 70 nA is reached. Discrete steps of 25 V are used between 200 and 450 V, and in steps of 50 V between 450 and 900 V. The high voltage setting is stored in a table and used during the actual measurement. Gain adjustment with the H6780-20 PMT module causes an additional 200 ms settling time.

The dc anode current, active source, active wavelength, and high voltage are displayed on the screen by the main control program. The temperature is stabilized with a discrete-time proportional-integral algorithm in a separate program running in the background.

Additional software may be run to record data from an AS/3 monitor (Datex-Ohmeda/GE Healthcare) including the heart beat, arterial oxygen saturation, and gas parameters of inhaled and exhaled air. In brain activation studies, sensory stimuli to the subject are controlled by a secondary PC running the presentation[20] software. A video capture system and an acceleration sensor are available to detect motion artifacts and monitor the subject's behavior in a darkened room.

F. Practical considerations

In difference imaging, the pre-scan is performed for the reference phantom only, and the actual measurement of the inhomogeneous tissue or phantom is made using the stored high voltage table. The effect of calibration errors is thus avoided when difference imaging is used.

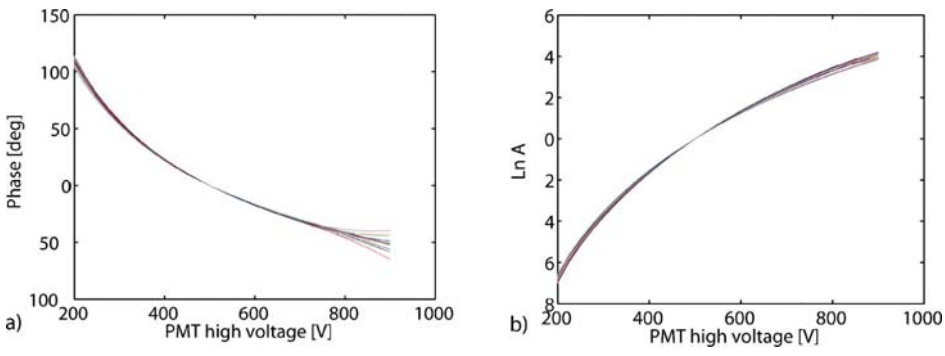

FIG. 3. (Color online) High-voltage calibration tables for (a) phase, (b) the logarithm of amplitude. The separate lines correspond to the 16 detectors.

Interchannel cross talk may result from light leak within the source fiber switches and electrical cross talk between the measurement channels. In order to minimize detector cross talk, a pseudo-differential amplifier was used and two analog-to-digital converter channels were used to record the signal from each detector channel. The radio frequency shielding used to prevent cross talk between the electronics modulating the intensity of the light sources and the detecting electronics is also sufficient to prevent interchannel cross talk in the radiofrequency system. In order to minimize the effect of interchannel cross talk in a tomographic measurement, the ordering of the optical fibers should be such that adjacent fibers correspond to adjacent physical channels on the ADC card. It is preferable to avoid a very close source-detector spacing since the gradient of the fluence is large near the source. Even though the PMT is not harmed by the measurements near the source if a low gain is used, the stability of PMT output signal is reduced by the light pulses which have a relatively large intensity.

III. CALIBRATION

The calibration of the data consists of three steps. Each calibration measurement is performed separately for both wavelengths.

Step 1—High voltage calibration. The amplitude and phase of the measured signal are measured as a function of the high voltage. A convenient way to obtain these measurements is by arranging the source and detector fibers in sequential order around a cylindrical phantom, and measuring the amplitude and phase for all the sources and detectors at all high voltages which produce an anode current below 80 nA. The high voltage is changed in 20 steps between 200 and 900 V using a measurement time of 5 s for each step. From the measurements, the changes in phase and ln A due to changes in the high voltage are used to build the calibration table for each detector. The phase and amplitude offsets due to each change in high voltage are averaged over the measurements which correspond to those source positions that produce a detected signal amplitude which is within the differential dynamic range of the system. Measurements in which the dc anode current are below 2 nA or above 80 nA excluded from the averaging as unreliable. The complex high voltage calibration table is normalized to 1 at the high voltage setting used for the absolute calibration (step 3) so that the effect of the high voltage on the absolute calibration measurement itself does not need to be corrected for high voltage dependency. The resulting phase and amplitude calibration tables for each detector for 760 nm are shown in Fig. 3.

Using a 5 s measurement time for each source-detector pair and high voltage setting, it is preferable to make two scans to improve the signal-to-noise ratio of the measurements. The mean standard deviation of the values in the resulting averaged high voltage table is 0.003 in ln A and 0.1° in phase. The instrument should be warmed up for ~1 h before the calibration table is measured.

Step 2—Interchannel offset calibration. Each source and detector channel has a different intrinsic attenuation and phase delay. These quantities are measured indirectly taking advantage of the rotational symmetry of a homogeneous cylindrical phantom. The method we use has been described in Ref. 21. The source and detector fibers are positioned at equal intervals in the order $\{D_1,S_1,D_2,S_2,\ldots,D_{16},S_{16}\}$ and the amplitude and phase for all source-detector pairs are measured. The intrinsic phase delays η_i and attenuations y_i of the phantom for those source-detector pairs which can be transformed from each other by a rotation (the group is denoted by the index i) are equal. The model data $X^*=\{x^*_{s,d}\}=\{y^*_{s,d}e^{j\phi^*_{s,d}}\}$ may be written in the form

$$
\begin{aligned}
X^* &= \begin{pmatrix} x^*_{1,1} & x^*_{2,1} & \cdots & x^*_{16,1} \\ x^*_{1,2} & x^*_{2,2} & \cdots & x^*_{16,2} \\ \vdots & \vdots & & \vdots \\ x^*_{1,16} & x^*_{2,16} & \cdots & x^*_{16,16} \end{pmatrix} \\
&= \begin{pmatrix} d_1 e^{j\delta_1} & & \\ & \ddots & \\ & & d_m e^{j\delta_{16}} \end{pmatrix} \\
&\quad \times \begin{pmatrix} y_1 e^{j\eta_1} & y_m e^{j\eta_{16}} & \cdots & y_2 e^{j\eta_2} \\ y_2 e^{j\eta_2} & y_1 e^{j\eta_1} & & y_3 e^{j\eta_3} \\ \vdots & \vdots & & \vdots \\ y_{16} e^{j\eta_{16}} & y_{15} e^{j\eta_{15}} & \cdots & y_1 e^{j\eta_1} \end{pmatrix} \\
&\quad \times \begin{pmatrix} s_1 e^{j\sigma_1} & & \\ & \ddots & \\ & & s_{16} e^{j\sigma_{16}} \end{pmatrix}, \qquad (1) \\
&= DYS
\end{aligned}
$$

where D and S are diagonal matrices which contain the detector and source attenuations and phase shifts on the diagonal and Y is a matrix that contains the attenuations and phase shifts due to the phantom. We define the relative calibration parameters as $\tilde{d}_i=d_i/d_1$, $\tilde{s}_i=s_i/s_1$, $\tilde{\delta}_i=\delta_i-\delta_1$, and $\tilde{\sigma}_i=\sigma_i-\sigma_1$. The parameters can be determined by minimizing the expressions

$$\|\ln|X| - \ln|G| - \ln|X^*(y,\tilde{s},\tilde{d})\|^2_{\mathrm{Frob}} \qquad (2)$$

and

$$\|\arg X - \arg G - \arg X^*(\eta,\tilde{\sigma},\tilde{\delta})\|^2_{\mathrm{Frob}} \qquad (3)$$

by varying the values of the relative calibration parameters for $i=2,\ldots,16$. Above, $X=\{x_{s,d}\}=\{y_{s,d}e^{j\phi_{s,d}}\}$ is a 16×16 matrix containing the measured data, and $G=\{g_{s,d}\}$ is a matrix which corrects for the PMT gain (step 1). The minimization problem is solved by Gauss–Newton iteration.

Step 3—Absolute calibration. As a final step, the phase and amplitude for source 1 and detector 1 are calibrated using an absolute calibration tool which has a known delay and fixed attenuation.[15,22]

The calibrated data X' can be calculated in complex form as

$$\ln X' = \ln X - \ln G - U \ln \tilde{s} - U \ln \tilde{d} - U \ln c + U \ln c', \tag{4}$$

where the 16×16 matrix X contains the measured data, G is the gain correction matrix, U is a 16×16 matrix with all elements equal to 1, $\ln c$ consists of the measured amplitude and phase from the absolute calibration tool using source 1 and detector 1, and c' contains the actual physical amplitude and phase values for the tool. Finally, calibrated phase and amplitude are obtained from

$$\phi = \arg X' \tag{5}$$

and

$$A = \exp|X'|. \tag{6}$$

IV. MODELING AND IMAGE RECONSTRUCTION

Image reconstruction in optical tomography requires the simultaneous recovery of the unknown spatial distribution of absorption and scattering parameters from boundary measurements. This is a nonlinear inverse problem, which can be formulated as a regularized optimization problem of recovering the coefficients $x(\mathbf{r}) = \{\mu_a(\mathbf{r}), \mu_s'(\mathbf{r})\}$ of a light transport model $f[x]$ which minimize the difference between the measured data y and the projection data f, expressed in the form of a suitable objective function.

In this article we employ the TOAST reconstruction package developed at University College London. It uses a finite element model to numerically solve the diffusion approximation to the radiative transfer equation. The inverse problem is solved iteratively with a regularized Gauss–Newton solver. For the reconstructions discussed in this article, we used a first order Tikhonov regularization where the hyperparameter is obtained from simulated data by an L-curve method.

The finite element method (FEM) forward model subdivides the volume into tetrahedral elements, defining a piecewise polynomial basis. The reconstruction is performed on a separate, regular basis of lower resolution. The FEM model of the cylindrical phantom discussed in this article consists of an unstructured mesh with 1.7×10^5 nodes and 1.2×10^5 ten-noded tetrahedral elements. The reconstruction is performed in a $12 \times 12 \times 12$ regular grid with tri-linear shape functions.

To match the model data, which are normalized to a source strength of 1, to the experimental data, the measured log amplitude data is shifted by a global constant. The constant can be determined by calculating the difference of the mean values of the model-predicted and measured log amplitude and phase data. The initial global model parameters (μ_a and μ_s') are determined by plotting the measured and model-predicted log amplitude data sets as a function of the optode spacing. The parameters are adjusted until the slopes match, and the log amplitude and phase shift terms are calculated. This factor can alternatively be determined during the reconstruction process, or it can be predetermined by applying the above procedure to data measured from a homogenenous phantom. The first method was used to make the images in this article, although the other methods yield similar images. It is our initial experience that this shift term is dependent on the optical properties of the measured object. In the future, more accurate source and detector models may be developed which make the coupling factor independent of the optical properties of the underlying tissue.[23] A more complete reconstrution of the coupling coefficients may be used to compensate for the effects of hair if present on the skin.[24]

To generate reference images for comparison with the experimental images, we calculated simulated data using a slightly different mesh of similar density. Reconstructions were calculated based on the simulated data with the same algorithm and parameters which were used for measured data.

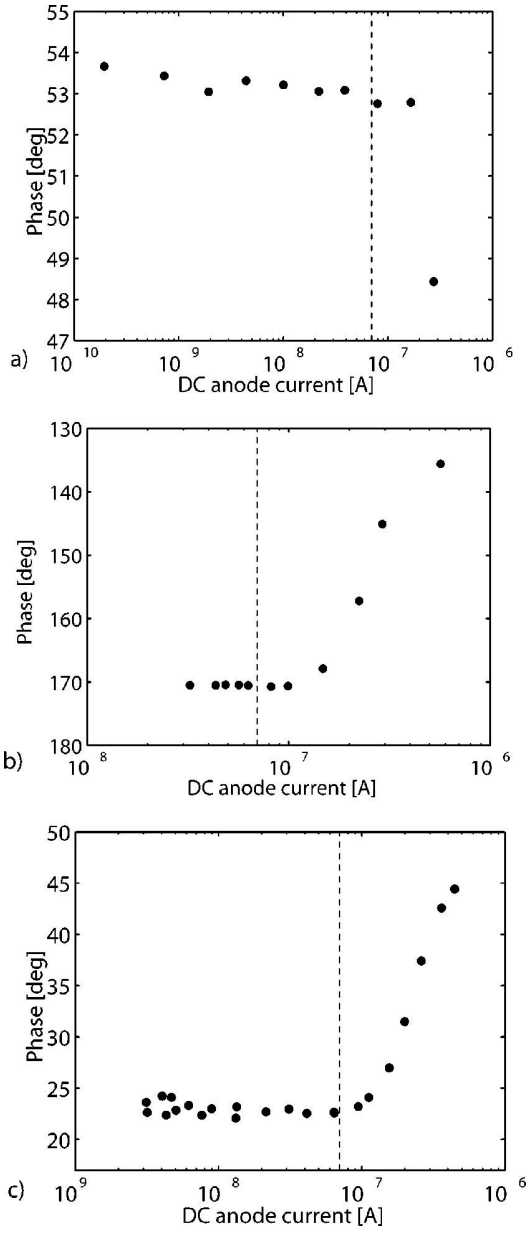

FIG. 4. Phase-amplitude cross talk. The measured uncalibrated phase is given as a function of dc anode current at a high voltage setting of (a) 300 V, (b) 600 V, and (c) 900 V. The pre-scan target is marked with a vertical line.

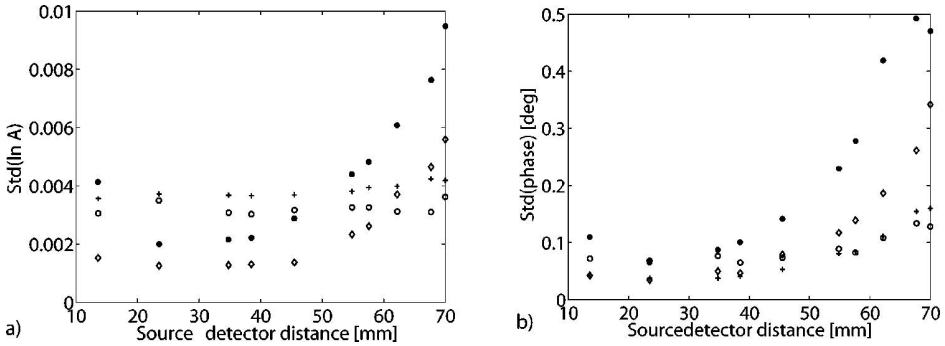

FIG. 5. Short-term repeatability as a function of source-detector distance and measurement time per source at a source power of 8 mW. (a) ln A, (b) phase. Measurement time=10 s per source (open dot), 5 s ("+"), 2 s (diamond), and 1 s (filled dot).

V. PERFORMANCE

A. Phase-amplitude cross talk

In order to evaluate the need to compensate for phase-amplitude cross talk, the dependency of phase on the intensity of the incident light was studied using a setup described in Ref. 15. Measurements at 300, 600, and 900 V with detector 1 are shown in Fig. 4. The measurements were made using channel 1 while the other detectors were at zero gain.

For reference, when the intensity of light striking the detector at 900 V is 1 pW, the anode current is approximately 50 nA. If the instrument is operated so that the anode currents remain below 80 nA, phase-amplitude cross talk has negligible effect on the quality of the measured phase. The negative slope at small anode currents at 300 V shown in Fig. 5(a) is due to light hysteresis, and it is not related to phase-amplitude cross talk.

B. Detector interchannel cross talk

In a multichannel measurement, interchannel cross talk can distort the measured amplitude and phase if the amplitudes on adjacent channels are of different orders of magnitude. This phenomenon was studied by measuring the effect of a large signal ($\sim$1 V) on channel 4, while the other channels were measured but the detectors of the other channels were shielded from light. The signal changes in channels 1, 2, 3, 5, and 6 were monitored and the activation of the light source on detector channel 4 was found to have no measurable effect on the amplitude on the other channels. The conclusion is that the current pseudo-differential amplifier configuration is sufficient to prevent interchannel cross talk between the detecting channels from the point of view of a practical measurement.

C. Source interchannel cross talk

According to the manufacturer's specifications,[25] the cross talk between the source fibers in the DiCon 1×16 switch is at most $1:10^{-8}$. In the phantom used in Sec. VI, the dynamic range in ln A is approximately 10. Thus, the maximum effect on the measured amplitude due the cross talk in the 1×16 switch is $A_{\mathrm{ct}}=10^{-8}\cdot\exp(10)\approx0.02\%$.

The cross talk from the 1×2 prism switch is at most 10^{-7} according to the manufacturer's specifications. Provided that the intensities from the lasers are of the same order of magnitude, in practice the wavelength dependence of the tissue attenuation is sufficiently small that the effects of this cross talk are negligible.

D. Noise and stability

To study the noise and stability of the system in a realistic situation, a homogeneous cylindrical phantom of 70 mm in diameter was measured repeatedly. The repeatability of each source-detector pair was calculated as the standard deviation of phase and ln A for the first six consequtive imaging cycles. The repeatability study was made separately for total measurement times (including all 16 sources) of 16, 32, 80, 160, and 480 s using an optical power of 8 mW. The mean of standard deviations over the measurements at the different source-detector separations is illustrated in Fig. 5.

Increasing the imaging time reduces noise at long distances but it increases the effect of the signal drift on the data and this causes the relatively large standard deviations at short distances. The repeatability can be enhanced further by increasing the laser power by up to 20 mW, which should be safe for most tissue studies. Additional improvement at long distances may be obtained by implementing an active cooling system for the PMTs.

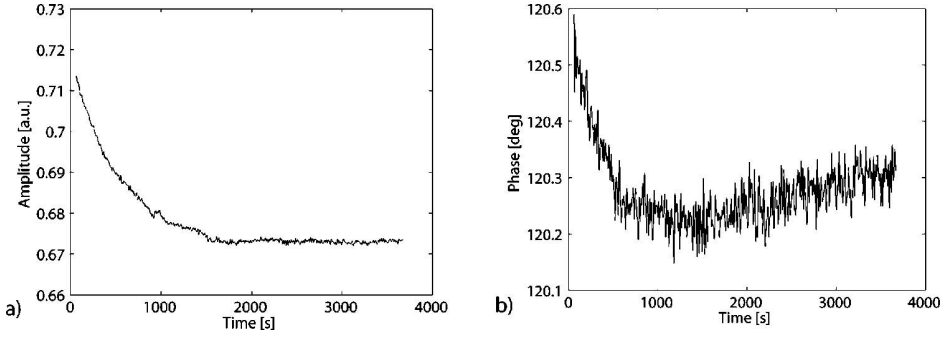

FIG. 6. (a) Amplitude, (b) phase during system warm-up.

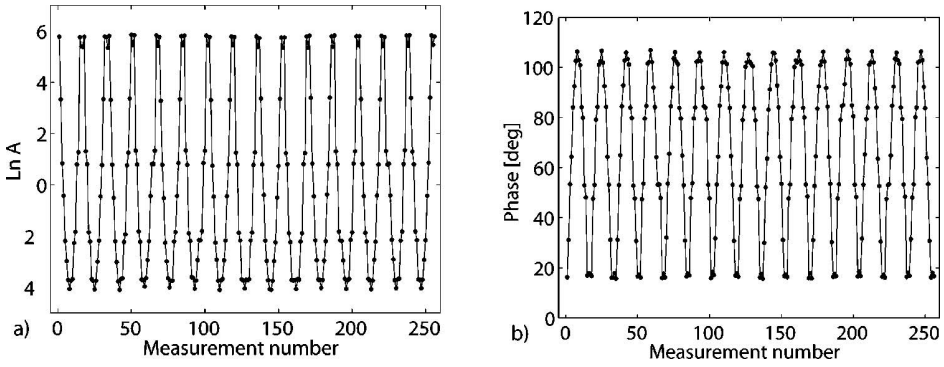

FIG. 7. Calibrated data from a homogeneous cylindrical phantom (a) ln A, (b) phase.

The system warm-up behavior is illustrated in Fig. 6. The amplitude and phase were measured during the first hour after system startup using a continuous measurement without source multiplexing. The warm-up time of the system can be estimated to be approximately 30 min.

The drift of the system was measured during an imaging sequence with a 5 s measurement time per source repeated continuously for a duration of 1 h. The drift was found to be $\sim 1\%/\mathrm{h}$ in amplitude and $\sim 0.05^{\circ}/\mathrm{h}$ in phase.

E. Dynamic range

The lower end of the dynamic range of the system is determined by noise. Amplitude SNR ~ 1 at 1 fW using a bandwidth of 1 Hz. The upper end of the dynamic range is limited by the PMT gain at 200 V. If we consider the high end of the dynamic range to be the intensity which causes a dc anode current of 80 nA at 200 V, which is approximately 30 nW, the overall dynamic range for the system is approximately $3 \cdot 10^7$. If the intensity of light is lower than 1 fW, the amplitude cannot be separated from the noise, and if the anode current at 200 V is higher than 80 nA, phase-amplitude cross talk is expected to distort the values of phase.

VI. PHANTOM EXPERIMENTS

A. Calibrated data from a homogeneous cylindrical phantom

A homogeneous solid resin cylinder of 7 cm diameter was measured with the system. The calibrated data are shown in Fig. 7. The optical fibers were placed in two rings at $z=+6$ mm and $z=-6$ mm from the center of the phantom.

B. Reconstruction of optical properties of inhomogeneous phantoms without reference data

Two cylindrical phantoms with perturbations in a homogeneous background were measured using the system. The optical fibers were placed in two rings, with eight source and

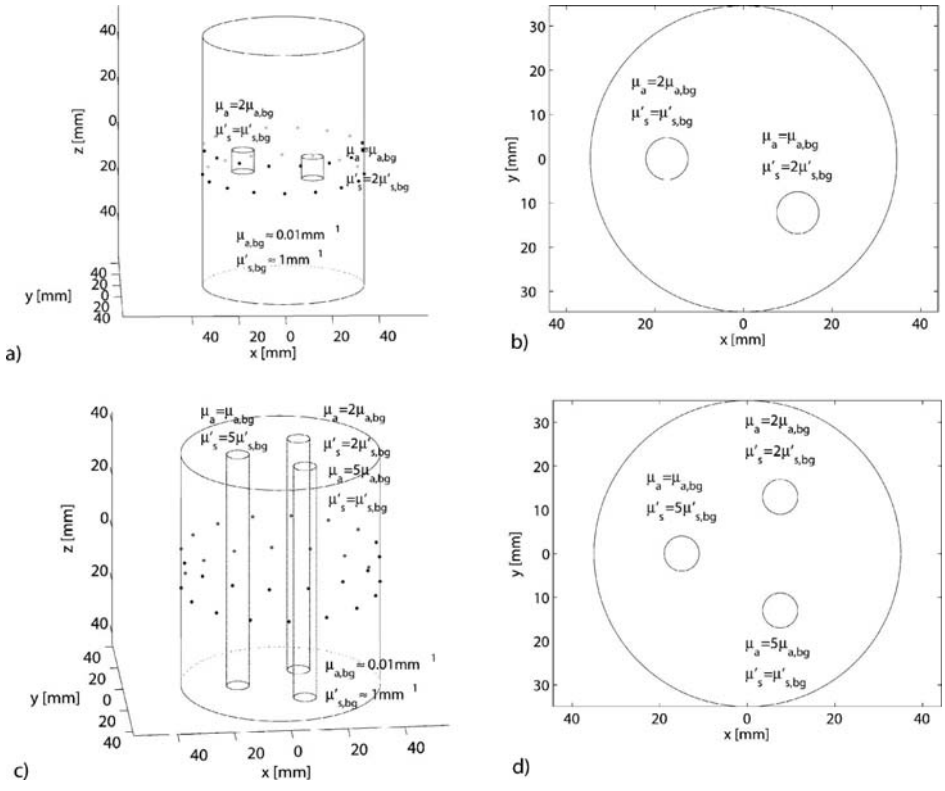

FIG. 8. Geometry and contents of (a) phantom A in 3D, (b) the *xy* plane ($z=0$) of phantom A, (c) phantom B in 3D, and (d) the *xy* plane ($z=0$) of phantom B.

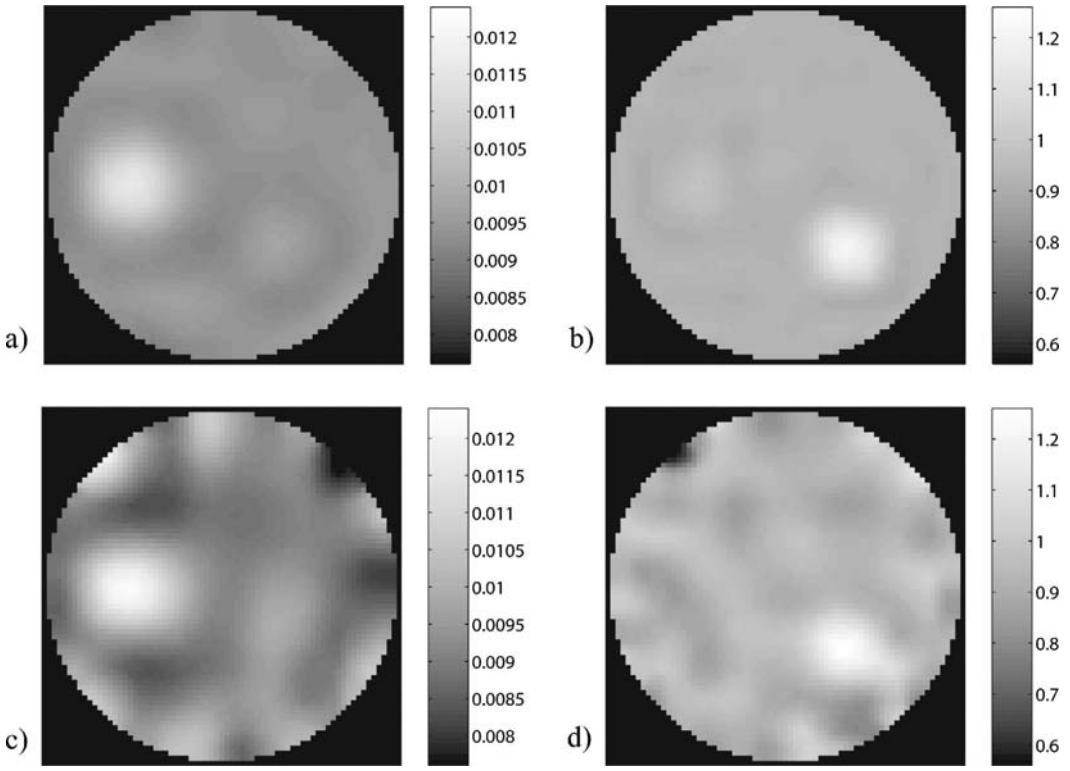

FIG. 9. Cross-sectional image of (a) absorption (simulated data), (b) scatter (simulated data), (c) absorption (measured data), (d) scatter (measured data) through the center of phantom A.

detector fiber bundles in each ring. The background optical properties of both phantoms were approximately $\mu_s' = 1\ \mathrm{mm}^{-1}$, $\mu_a = 0.01\ \mathrm{mm}^{-1}$, $n = 1.56$, and $g = 0.5$. Phantom A had two small cylindrical targets with optical properties of $(\mu_a, 2\mu_s')$ and $(2\mu_a, \mu_s')$ relative to the background. Both the height and diameter of the targets were 9.5 mm. Phantom B had three rods with optical properties of $(\mu_a, 5\mu_s')$, $(2\mu_a, 2\mu_s')$, and $(5\mu_a, \mu_s')$ relative to the background.[26] Illustrations of the two phantoms are given in Fig. 8. The positions of the optical fiber bundles are marked with dots, with eight sources and eight detectors in each of two rings separated by 12 mm in the z direction.

The system was calibrated using a homogeneous cylindrical phantom according to the method described in Sec. III. The optical properties of the homogeneous phantom were different from phantoms A and B, and the actual measurements were made with a different ordering of the source and detector fibers in order to test the generalization performance of the system.

Three-dimensional (3D) images of μ_a and μ_s' were reconstructed using the calibrated data and the central cross sections are shown in Figs. 9(c), 9(d), 10(c), and 10(d). Corresponding images calculated from simulated data are shown in Figs. 9, 10(a), and 10(b).

The targets in both phantoms were reconstructed successfully and without substantial cross talk between the parameters apart from the case of the highly absorbing rod in Phantom B. This rod is visible in the reconstructed scattering image in both simulated and measured cases [Figs. 10(b) and 10(d)]. In this instance, the inter-parameter cross talk could be reduced by increasing the number of source and detector channels in the system. The optical property values reconstructed from measured data are remarkably similar to the values obtained from simulated data. The contrasts in the reconstructed images of the targets are lower than the true contrasts because of the small size of the targets. The artifacts in the images near the boundary of the phantom may be reduced by using an algorithm which reconstructs the coupling coefficients between each optical fiber and the phantom together with the optical properties. However, in this case, a normal reconstruction of μ_a and μ_s' was used to show the magnitude of the calibration artifacts. The high apparent scattering coefficient on the boundary of Phantom B in Fig. 10(d) is probably due to reflections between the fiber-holding ring and the phantom surface. Black velvet was used to prevent this phenomenon in the measurement of Phantom A.

The quality of the reconstructed images from Phantom A is similar to what has been achieved with the system using difference imaging. This indicates that the calibration procedure works as intended and the quality of the calibrated data is sufficient for practical applications. The image quality is not reduced due to the absence of the reference phantom provided that the target contrast is sufficient, and that the coordinates of the optode positions and the geometry of the object are known accurately. To compensate for imprecise knowledge of the geometry, new reconstruction techniques have been developed.[27,28] The phantoms used in this study provide a verification of the accuracy of the system but they do not require the use of the full dynamic range. In practical use, tissues having larger diameters are often studied.

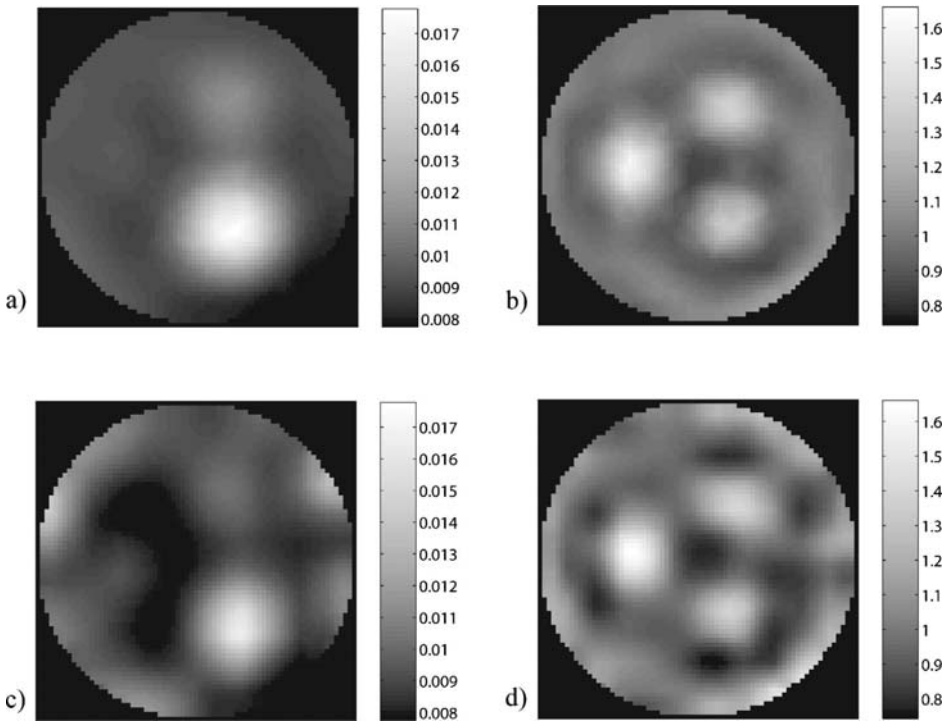

FIG. 10. Cross-sectional image of (a) absorption (simulated data), (b) scatter (simulated data), (c) absorption (measured data), (d) scatter (measured data) through the center of phantom B.

VII. DISCUSSION

An intensity modulated optical tomography system with 16 sources and detectors has been developed. Of particular interest is the ability of the system to feature a wide dynamic range of detected intensities without the use of variable optical attenuators. Factors affecting the quality of data such as noise, interchannel cross talk, phase-amplitude cross talk, and system stability were discussed in detail. A three-step method was used to calibrate the phase and amplitude measurements so that the effects of different offsets and gain responses of the different channels are compensated for. This allows the use of the measurements for the imaging of the optical properties of the tissue without the use of a reference measurement on a homogeneous phantom which has a similar geometry and optical properties to the tissue. Images of scatter and absorption in two solid phantoms were reconstructed using calibrated data.

Previously, difference imaging has been used to reconstruct the optical properties of phantoms using time-resolved instrumentation by Hebden *et al.*[29] and frequency-domain instrumentation, e.g., by McBride *et al.*[10] Absolute imaging of a phantom with high-contrast targets has been demonstrated using time-resolved data by Arridge *et al.*[30] The advantage of the method described in this article is that it can be used to make high-quality images of the optical properties of phantoms with small targets having realistic optical properties and target-to-background contrasts without the use of a homogeneous reference phantom. The reconstructed images show the internal optical properties of the phantoms fairly accurately, considering the small size of the perturbations and the limited number of sources and detectors available in the prototype.

The instrumentation and methods described in this article may be applied to the imaging of the concentrations of oxy- and deoxyhemoglobin in infant brains, muscle tissue, and with the implementation of an appropriate interface between the patient and the optical fibers, mammography. Activation studies of adults and neonates are also possible. Planned improvements in the system include the incorporation of higher-power laser diodes and a faster switch for the time multiplexing of the source fibers.

ACKNOWLEDGMENTS

The authors would like to thank the Jenny and Antti Wihuri Foundation, the Academy of Finland (Project Nos. 29820, 200522, and 206449), the graduate school Functional Studies in Medicine, the Foundation of Technology (TES), the Finnish Cultural Foundation, the Instrumentarium Science Foundation, the Emil Aaltonen Foundation, and the National Technology Agency of Finland (TEKES) for their financial support, and Professor Jeremy Hebden for providing the phantoms used in this study.

[1] S. R. Arridge, Inverse Probl. **15**, R41 (1999).
[2] J. C. Hebden, Psychophysiology **40**, 501 (2003).
[3] I. Nissilä, T. Noponen, J. Heino, T. Kajava, and T. Katila, *Advances in Electromagnetic Fields in Living Systems*, edited by J. Lin (Springer, Berlin, 2005).
[4] S. R. Arridge and W. R. B. Lionheart, Opt. Lett. **23**, 882 (1998).
[5] V. Ntziachristos, X. Ma, and B. Chance, Rev. Sci. Instrum. **69**, 4221 (1998).
[6] V. Ntziachristos, V. X. H. Ma, A. G. Yodh, and B. Chance, Rev. Sci. Instrum. **70**, 193 (1999).
[7] D. Grosenick, H. Wabnitz, H. H. Rinneberg, K. T. Moesta, and P. M. Schlag, Appl. Opt. **38**, 2927 (1999).
[8] H. Eda, I. Oda, Y. Ito, Y. Wada, Y. Oikawa, Y. Tsunazawa, M. Takada, Y. Tsuchiya, Y. Yamashita, M. Oda, A. Sassaroli, Y. Yamada, and M. Tamura, Rev. Sci. Instrum. **70**, 3595 (1999).
[9] F. E. W. Schmidt, M. E. Fry, E. M. C. Hillman, J. C. Hebden, and D. T. Delpy, Rev. Sci. Instrum. **71**, 256 (2000).
[10] T. O. McBride, B. W. Pogue, S. Jiang, U. L. Österberg, and K. D. Paulsen,

Rev. Sci. Instrum. **72**, 1817 (2001).
[11] B. Chance, M. Cope, E. Gratton, N. Ramanujam, and B. Tromberg, Rev. Sci. Instrum. **69**, 3457 (1998).
[12] N. Ramanujam, C. Du, H. Y. Ma, and B. Chance, Rev. Sci. Instrum. **69**, 3042 (1998).
[13] Y. Yang, H. Liu, X. Li, and B. Chance, Opt. Eng. (Bellingham) **36**, 1562 (1997).
[14] S. Fantini, M.-A. Franceschini-Fantini, J. S. Maier, S. A. Walker, B. Barbieri, and E. Gratton, Opt. Eng. (Bellingham) **34**, 32 (1995).
[15] I. Nissilä, K. Kotilahti, K. Fallström, and T. Katila, Rev. Sci. Instrum. **73**, 3306 (2002).
[16] T. H. Pham, O. Coquoz, J. B. Fishkin, E. Anderson, and B. J. Tromberg, Rev. Sci. Instrum. **71**, 2500 (2000).
[17] M. Cope, Ph.D. thesis, University College London, 1991.
[18] C. H. Schmitz, M. Löcker, J. M. Lasker, A. H. Hielscher, and R. L. Barbour, Rev. Sci. Instrum. **73**, 429 (2002).
[19] A. M. Siegel, J. J. A. Marota, and D. A. Boas, Opt. Express **4**, 287 (1999).
[20] Available at http://www.neuro-bs.com
[21] T. Tarvainen, V. Kolehmainen, M. Vauhkonen, A. Vanne, A. Gibson, S. R. Arridge, M. Schweiger, and J. P. Kaipio, Appl. Opt. (accepted).
[22] E. M. C. Hillman, J. C. Hebden, F. E. W. Schmidt, S. R. Arridge, M. Schweiger, H. Deghani, and D. T. Delpy, Rev. Sci. Instrum. **71**, 3415 (2000).
[23] T. Tarvainen, M. Vauhkonen, V. Kolehmainen, and J. P. Kaipio, Appl. Opt. **44**(6), 876 (2005).
[24] D. A. Boas, T. Gaudette, and S. R. Arridge, Opt. Express **8**, 263 (2001).
[25] DiCon VX500 $1\times N$ datasheet, available at http://www.diconfiberoptics.com (May 2004).
[26] J. C. Hebden, F. E. W. Schmidt, M. E. Fry, M. Schweiger, E. M. C. Hillman, D. T. Delpy, and S. R. Arridge, Opt. Lett. **24**, 534 (1999).
[27] J. Heino, E. Somersalo, and J. P. Kaipio, Opt. Express **13**, 296 (2004).
[28] J. J. Stott, J. P. Culver, S. R. Arridge, and D. A. Boas, Appl. Opt. **42**(16), 3154 (2003).
[29] J. C. Hebden, H. Veenstra, H. Dehghani, E. M. C. Hillman, M. Schweiger, S. R. Arridge, and D. T. Delpy, Appl. Opt. **40**, 3278 (2001).
[30] S. R. Arridge, J. C. Hebden, M. Schweiger, F. E. W. Schmidt, M. E. Fry, E. M. C. Hillman, H. Dehghani, and D. T. Delpy, Int. J. Imaging Syst. Technol. **11**, 2 (2000).